Ultrasonics 70 (2016) 275–283

Contents lists available at ScienceDirect

Ultrasonics

journal homepage: www.elsevier.com/locate/ultras

Investigation of polymer-shelled microbubble motions in acoustophoresis

Satya V.V.N. Kothapalli [a], Martin Wiklund [b], Birgitta Janerot-Sjoberg [a,d,e], Gaio Paradossi [c], Dmitry Grishenkov [a,d,e,*]

[a] Department of Medical Engineering, School of Technology and Health, KTH Royal Institute of Technology, SE-142 51 Stockholm, Sweden
[b] Department of Applied Physics, KTH—Royal Institute of Technology, SE-106 91 Stockholm, Sweden
[c] Dipartimento di Chimica, Università di Roma Tor Vergata, 00133 Rome, Italy
[d] Department of Clinical Science, Intervention and Technology, Karolinska Institute, SE-142 51 Stockholm, Sweden
[e] Department of Clinical Physiology, Karolinska University Hospital, SE-142 51 Stockholm, Sweden

ARTICLE INFO

Article history:
Received 10 June 2015
Received in revised form 30 March 2016
Accepted 19 May 2016
Available online 1 June 2016

Keywords:
Acoustophoresis
Ultrasound contrast agent
Radiation force
Ultrasound standing wave
Acoustic contrast factor

ABSTRACT

The objective of this paper is to explore the trajectory motion of microsize (typically smaller than a red blood cell) encapsulated polymer-shelled gas bubbles propelled by radiation force in an acoustic standing-wave field and to compare the corresponding movements of solid polymer microbeads. The experimental setup consists of a microfluidic chip coupled to a piezoelectric crystal (PZT) with a resonance frequency of about 2.8 MHz. The microfluidic channel consists of a rectangular chamber with a width, w, corresponding to one wavelength of the ultrasound standing wave. It creates one full wave ultrasound of a standing-wave pattern with two pressure nodes at $w/4$ and $3w/4$ and three antinodes at 0, $w/2$, and w. The peak-to-peak amplitude of the electrical potential over the PZT was varied between 1 and 10 V. The study is limited to no-flow condition. From Gor'kov's potential equation, the acoustic contrast factor, Φ, for the polymer-shelled microbubbles was calculated to about -60.7. Experimental results demonstrate that the polymer-shelled microbubbles are translated and accumulated at the pressure antinode planes. This trajectory motion of polymer-shelled microbubbles toward the pressure antinode plane is similar to what has been described for other acoustic contrast particles with a negative Φ. First, primary radiation forces dragged the polymer-shelled microbubbles into proximity with each other at the pressure antinode planes. Then, primary and secondary radiation forces caused them to quickly aggregate at different spots along the channel. The relocation time for polymer-shelled microbubbles was 40 times shorter than that for polymer microbeads, and in contrast to polymer microbeads, the polymer-shelled microbubbles were actuated even at driving voltages (proportional to radiation forces) as low as 1 V. In short, the polymer-shelled microbubbles demonstrate the behavior attributed to the negative acoustic contrast factor particles and thus can be trapped at the antinode plane and thereby separated from particles having a positive acoustic contrast factor, such as for example solid particles and cells. This phenomenon could be utilized in exploring future applications, such as bioassay, bioaffinity, and cell interaction studies *in vitro* in a well-controlled environment.

1. Introduction

In a current clinical practice a suspension of micro-size gas core bubbles is used as and efficient ultrasound contrast agent (UCA) [1]. As early as 1968 Gramiak and Shah [2] demonstrated the enhancement of the image contrast in echocardiographic study of aorta following the injection of the suspension of agitated saline solution containing free gas bubbles. In order to increase stability of the free gas bubbles, otherwise dissolving in a surrounding media in fractions of a second, the gas core were encapsulated within the solid shell. The solid encapsulating shell is typically made of albumin protein [3], phospholipids [4], or polymers [5]. Moreover, the outermost surface of the encapsulating shell can be further modified to accommodate ligands, pharmacological molecules or genes for molecular imaging and localized drug delivery [6–8]. In these applications the acoustic radiation force which propels and accumulates the

---

* Corresponding author at: Department of Medical Engineering, School of Technology and Health, KTH Royal Institute of Technology, Alfred Nobels allé 10, SE-142 51 Stockholm, Sweden.

E-mail address: dmitryg@kth.se (D. Grishenkov).

http://dx.doi.org/10.1016/j.ultras.2016.05.016
0041-624X/© 2016 Elsevier B.V. All rights reserved.

free-circulating in blood stream bubbles on the target is of particular interest [9,10].

For more than a century, researchers have been exploring the effects of acoustic radiation force on particles suspended in liquid media and the particles' motion with the acoustic waves [11]. In the last two decades, several medical innovations have been based on this acoustic radiation-force phenomenon, including vibro-acoustography [12], shear wave elastography [13], acoustic radiation-force impulse imaging [14], magnetic resonance acoustic radiation-force imaging [15], the assessment of the viscoelastic properties of tissue [16], and the precise manipulation of cells or particles in a standing wave [17]. This study focuses on the application of acoustic radiation forces acting on microbubbles in standing-wave (stationary sound fields) acoustic fields. Blake [18] reported that millimeter-size gas bubbles (resonance frequency was well below the excitation frequency) suspended in a liquid were drawn to the pressure antinodes by the radiation force in a standing wave. The bubbles coalesced owing to the secondary radiation effect (also known as Bjerknes force) when they moved close to each other and merged into a larger bubble with a lower resonance frequency. Once the resonance frequency of a resulting bubble was comparable to the driving frequency, then it propelled away from the pressure antinode to the pressure node [19]. Apart from the frequency effect, acoustic pressure also plays significant roles in bubble motion. At a high enough acoustic pressure, even the driving frequency is well below the bubbles' resonance frequency, resulting in bubble translation and precision around the pressure node [20]. On the other hand, Kundt and Lehman demonstrated that when radiation force was exerted on solid Styrofoam chips, particles accumulated at the pressure nodes in acoustic standing-wave fields [21]. The motion of particles and their directions in a standing-wave acoustic field depend on several factors, such as driving frequency, size, density, and compressibility of the particle [22,23]. If the particle possesses greater compressibility and lower density than the surrounding liquid media, it tends to move toward the pressure antinode; otherwise, the particle moves toward the pressure node [22,23]. Note that this phenomenon is applicable only when the resonance frequency and size of the particle are well below the driving frequency and the wavelength of the incidental acoustic wave.

Based on particle responses upon the radiation force in acoustic standing-wave fields, the field of *acoustophoresis* (acoustic manipulation) has emerged. Acoustophoresis is an emerging clinical tool, especially in noncontact cell handling, useful for concentrating, sedimenting, sorting, and purifying [24–26]. Laurell et al. [27] successfully separated lipid particles from blood cells by using the acoustophoresis separation method. Analogously, the successful separation of platelets and serum from blood [28], the separation of lipid particles from milk [29], the separation of crude oil droplets from environmental water samples [30], and the separation of targeted cells with biofunctional elastomeric particles from nontargeted cells [31,32] have all been reported. Recently, tunable glass-shelled core (core: air, water, and steel) particles were also shown as negative acoustic contrast particles [33]. In that later study, the authors mentioned that the glass-shelled core-particle scenario can extend to UCAs but did not take this into account. Moreover, the authors did not mention the particular type of UCA that is, whether thin- or thick-shelled air-filled gas bubbles were used—nor did they report the type of shell material, such as lipids or polymers.

Thick- or thin-shelled microbubbles are defined based on the ratio between shell thicknesses and the total microbubble radius, where bubbles with a ratio below 5% are considered thin [34]. In the interest of studying sonoporation or cell lysis, Khanna et al. [35] introduced thin Albunex-shelled (human-protein-shelled) microbubbles (Optison®) and erythrocytes (red blood cells) simultaneously into ultrasound standing-wave fields at a frequency of about 1.5 MHz. The authors reported that in the presence of Optison®, the erythrocytes moved more vigorously and randomly in the acoustic field and released significant amounts of hemoglobin. However, the Optison® microbubbles also disappeared within the first frame—that is, within a few milliseconds. In the current study, we utilized thick-shelled polymer microbubbles with the ratio of shell thickness to microbubble radius above 5% [36]. Compared to the shell of lipid- or protein-shelled microbubbles [37,38], the thick encapsulated polymer shell offers increased mechanical stability resulting not only in shelf-life of several months but also in extended circulation time during in vivo tests. Thick shell also offers larger volume for incorporation of therapeutical gas [39] or pharmacological relevant molecules [39] to be delivered locally following ultrasound excitation.

The aim of the study was to investigate the movements of polymer-shelled air-core microbubbles induced by radiation force in acoustic standing-wave fields and to compare these with the corresponding movements of solid polymer beads, currently used as a blood mimicking phantom.

Prior to the experiments, we estimated the acoustic contrast factor, Φ, value of our polymer-shelled microbubbles suspended in water following the Gor'kov potential theory [22]. The sign Φ predicts the particle trajectory motion, which is extensively described in the theory section. Furthermore, the response of the polymer-shelled microbubbles at different driving voltages across the PZT is explored so as to identify the relation between acoustic pressure and the trajectory motion of the microbubbles. Our experimental results are compared with those presented in well-established studies of polymer microbeads [40,41]. Finally, the paper concludes with a thorough discussion of the fundamental physical principles behind the observed phenomena and notes potential applications for polymer-shelled microbubbles.

2. Theory

2.1. Radiation force

Suspended particles in a liquid experience both axial and transverse acoustic radiation forces when they are subjected to standing wave acoustic fields. The axial radiation force acts toward the direction of the wave propagation, which is responsible for a driving particle to either pressure node (velocity antinode) or pressure anti-node (velocity node). The transverse radiation force is acting perpendicular to the wave propagation, that is accountable for grouping the particles to clusters. The mathematical representation of the primary axial radiation force [22] is given in Eq. (1),

$$F^{rad} = -V\left[\frac{f_1}{2}\beta_s \nabla\langle p_1^2\rangle - \frac{3f_2}{4}\rho_s \nabla\langle v_1^2\rangle\right], \tag{1}$$

where V is the volume of the particle; $f_1 = 1 - \frac{\beta_p}{\beta_s}$ and $f_2 = \frac{2(\rho_p - \rho_s)}{2\rho_p + \rho_s}$ are the monopole and dipole scattering coefficients; ρ_p and ρ_s and β_p and β_s are the densities and compressibility of the particle and the surrounding media, respectively; p_1 is the incidental pressure; and v_1 is the velocity of the particle. In 2-D acoustophoresis, microparticles move in a horizontal direction, $x(t)$, and in a transversal direction, $y(t)$. The acoustic pressure field in transverse motion is $p_1 = p_a \cos(ky)$, and when this is substituted in Eq. (1), the radiation force acting on the transverse field becomes [42]

$$F_y^{rad} = \frac{4\pi}{3} k_y a^3 E_{ac} \Phi(\beta, \rho) \sin(2k_y y), \tag{2}$$

where $k(=2\pi/\lambda)$ is wavenumber; λ is the wavelength equal to channel width, w; a is the radius of the single spherical particle; E_{ac} is the time-averaged acoustic energy density; and $\Phi(\beta, \rho)$ is the acoustic contrast factor, which equals $\frac{1}{3}f_1 + \frac{1}{2}f_2$.

2.2. Acoustic contrast factor

The direction of particle movement depends on the sign of the acoustic contrast factor, Φ. As shown in Fig. 1, particles with a positive Φ are translated and focused at the pressure node (i.e., velocity antinode). Particles with a negative Φ move in the opposite direction and are trapped at pressure antinode (velocity node).

Barnkob et al. [40] estimated the Φ of polyamide microbeads suspended in water to about +0.24. Thus, microbeads are dragged into pressure nodes by the radiation force in a standing wave acoustic field. The polymer-shelled gas particle/bubble however, is a combination of a gas core and a complex polymer shell. Thus, the density is calculated by considering the cumulative sum of air core and polymer shell densities, which can be expressed as $\rho_p = \rho_{shell}(1 - \alpha^3) + \rho_{gas}\alpha^3$. Here the parameter α is the ratio between inner, R_{01} and outer, R_{02}, radii of the polymer-shelled gas particle, and equals 0.84. Fernandes et al. [43] reported that, the encapsulated PVA shell is the composition of 80% water and 20% PVA moieties. The density of PVA and water is about 1269 kg/m^3 and 1000 kg/m^3 respectively and the total shell density thereby equals 1053 kg/m^3. Thus the total density of the polymer-shelled gas particle, ρ_p, is 429.6 kg/m^3.

A pulsating microbubble in lower acoustic pressure can be modelled as a damped linear harmonic oscillator. Grishenkov et al. [36] derived the linearized version of the non-linear equation of motion of polymer-shelled microbubbles given in Eq. (3), which is similar to the damped harmonic oscillator model as given in Eq. (4),

$$\begin{aligned}&\left[-\omega^2 + j\tfrac{4}{\gamma\rho_S R_{01}^2 R_{02}^3}\left(R_{01}^3\mu_L\omega + V_S G''(\omega)\right)\right.\\&\left.+\tfrac{3}{\gamma\rho_S R_{01}^2}\left(\kappa P_{G,eq} + \tfrac{4V_S}{3R_{02}^3}G'(\omega)\right)\right]X(\omega) = \tfrac{\Delta\hat{P}}{\gamma\rho_S R_{01}^2},\end{aligned} \tag{3}$$

$$[-\omega^2 + 2j\delta\omega + \omega_0^2]X(\omega) = \frac{\Delta\hat{P}}{\gamma\rho_S R_{01}^2}, \tag{4}$$

where R_{01} and R_{02} are the inner and outer radii of the microbubble at rest; μ_L is the shear viscosity in surrounding liquid; p_0 is the ambient pressure; p_{ac} is an incidental acoustic pressure; $V_S = R_{02}^3 - R_{01}^3 = R_2^3 - R_1^3$ describes the shell incompressibility assumption in the model; $P_{G,eq}$ represents the gas pressure at equilibrium that is assumed to be equal to p_0; $G'(\omega)$ and $G''(\omega)$ are the frequency-dependent storage and loss modulus; ρ_s and ρ_L are the densities of shell and liquid; $\omega(=2\pi f)$ and $\omega_0(=2\pi f_0)$ are the particle's driving frequency and resonance frequency, respectively; and κ is the polytrophic gas constant that varies between 1 (isothermal) and 1.4 (adiabatic).

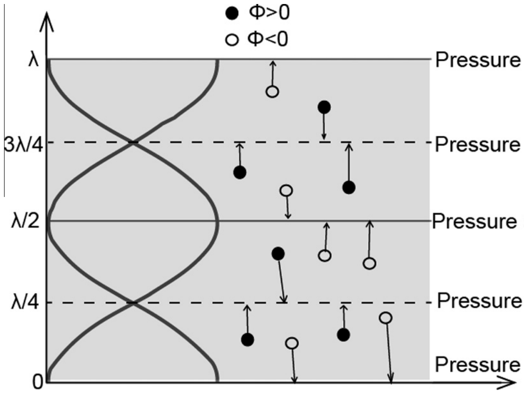

Fig. 1. Illustration of the acoustic pressure standing-wave profile and particle motion depending on different acoustic contrast factors, Φ, in a liquid suspension.

Comparing Eqs. (4) and (5) allows us to identify the mass $(m = \gamma\rho_S R_{01}^2)$, friction $\left(R = 2(R_{01}^3\mu_L\omega + V_S G''(\omega))/R_{02}^3\right)$, and stiffness $\left(K_P = \kappa P_{G,eq} + \frac{4}{3R_{02}^3}V_S G'(\omega)\right)$. Here, the storage modulus $G'(\omega)$ can be expressed as $G'(\omega) = G_{eq} + G_1\omega^{3/4}$, where G_{eq} is the equilibrium shear modulus and G_1 is the frequency-dependent shear modulus. Both G_{eq} and G_1 were identified by fitting theoretical attenuation spectra with measured attenuation spectra, which were reported as 10.5 MPa and 5.5 Pa/(rad/s)$^{3/4}$, respectively [44]. Herein the driving frequency, f, of PZT equals 2.8 MHz; therefore, G' is 11.9 MPa. The mean external radius of the bubble is 1.9 µm, and $P_{G,eq}$ is the atmospheric pressure—that is, about 10^5 Pa. The resultant K_p is equal to 12.2 MPa, and the inverse of K_p, the compressibility, β_p, is about 0.08 MPa^{-1}. Further, the monopole scattering coefficient or compressibility factor, f_1, would be 181.4, and the dipole scattering coefficient or density factor, f_2, would be +0.4. Thus, the acoustic contrast factor, or Φ value, is estimated to -60.7.

2.3. Transverse particle path, acoustic energy density and local pressure amplitude

The trajectory motion of the single particle, either microbubble or microbead, in acoustophoresis can be assessed using the equation for transverse particle part $y(t)$ where the expression for transverse radiation force (Eq. (2)) is balanced with the Stokes drag force [42]

$$y(t) = \frac{1}{k_y}\arctan\left\{\tan[k_y y(0)]\exp\left[\frac{4\Phi}{9\eta}(k_y a)^2 E_{ac} t\right]\right\}, \tag{5}$$

where $y(0)$ is the initial position of the particle at $t = 0$; and η is the viscosity of the surrounding liquid.

Inverting the Eq. (5) lead to expression for the acoustic energy density.

$$E_{ac} = \frac{9\eta}{4\Phi(k_y a)^2 t}\ln\left[\frac{\tan[k_y y(t)]}{\tan[k_y y(0)]}\right]. \tag{6}$$

Keeping in mind that both structural and mechanical characteristics of the microbeads are known [40] it is possible using the experimentally measured accumulation time, t, to estimate the value for acoustic energy density at different driving voltage. Furthermore the pressure amplitude, p_a, in a chip can be estimated from the relation $p_a = 2\sqrt{\rho_s c_s^2 E_{ac}}$, where ρ_s and c_s are the density and speed of sound of surrounding liquid.

Thus the indirect calibration of the acoustic standing-wave field can be achieved.

3. Material and method

3.1. Particles

In this research, two particle types were utilized namely, polymer microbeads and polymer-shelled microbubbles. The testified polymer microbeads' (polymer was made of polyamide molecules) suspension was prepared by adding a mixture of Milli-Q water (with 0.01% Tween20) to blood-mimicking fluid (EU-DFS-BMF-ver.1 for flow Doppler Phantoms, Danish Phantom Design, Denmark) in a ratio of 1:9. Barnkob et al. [45] reported that the concentration of microbeads suspension was about 3.5×10^{11} ml^{-1}, while its diameter was 4.5 ± 0.7 µm. The polymer-shelled microbubbles resulted from the encapsulation of microsize gas bubbles with a PVA (poly vinyl alcohol), hydrogel. The polymer-shelled microbubbles were reproduced in our lab following the protocol developed by Cavalieri et al. [37]. Concisely, the PVA powder (Sigma–Aldrich, Chemie GmbH, Germany) was dissolved in distilled water, and the resulting solution was mixed with sodium (meta)periodate at a temperature of 80 °C. Later, this solution was subjected to a homogenizer ULTRA-Turrax® (Ika, Germany) for two hours. During the high-stirring process, the polymer moieties with hydrophilic heads and hydrophobic tails were rearranged at the water/air interface. As a result, stabilized gas particles were obtained. The diameter and concentration of polymer-shelled microbubbles equal $3.8 \pm 0.6\ \mu m$ and $5 \times 10^8\ ml^{-1}$, respectively. The thickness of the polymer shell reported by Poehlmann et al. [44] was approximately 300 nm. Thus, the ratio of shell thickness to microbubble radius is 16%.

3.2. Experimental set-up

The schematic representation of the experimental setup is presented in Fig. 2. A microfluidic chip (GeSim GmbH, Dresden, Germany) made of a glass–silicon-glass composite structure [45] was placed under the transmission microscope (Axiovert 40 CFL, Carl Zeiss, USA). The microchip included the microfluidic channel and a rectangular chamber. The depth and width of the channel were about $110 \times 300\ \mu m^2$, and the length and width of the rectangular chamber were about $8900 \times 530\ \mu m^2$. The microchip had one inlet and one outlet. A PZT was coupled to the upper surface of the microchip using conductive adhesive gel (Tensive®, Laboratories, Inc., USA). An impedance analyzer (Model 16777k, Sine-Phase Instruments GmbH, Moedling, Austria) found the fundamental resonance frequency of the attached PZT to be 2.8 MHz.

The PZT was driven to operate by a function generator (AFG 3022, Tektronix Inc., USA) with a continuous sinusoidal wave. The width of the rectangular chamber was designed to equal one wavelength, λ, of the ultrasound standing wave—that is, 535 μm. Thus, the cage acted as a full wave resonator, and the superposition of vertical and horizontal waves in the full wave resonator resulted in two pressure node planes (at $\lambda/4$ and $3\lambda/4$) and three pressure antinode planes (at 0, $\lambda/2$, and λ). The microscope, equipped with a 10× objective (NA = 0.25; Zeiss, Germany), was focused on the rectangular chamber. Images were captured by a digital camera (SLT-A77V, 77α, Minato, Japan) with a frame rate of 50 Hz. In these experiments, the concentrations of both microbeads and polymer-shelled microbubbles were diluted with distilled water to equal $10^6\ ml^{-1}$. The solution was introduced into the channel through the inlet using a syringe (BD Luer-Lok™ Tip, Sweden). The flow of the particle suspension in the microchip was interrupted in order to bring the solution into a stationary position, thereby avoiding pressure gradient and microstreaming effects. Thus, all experiments were performed in no-flow conditions.

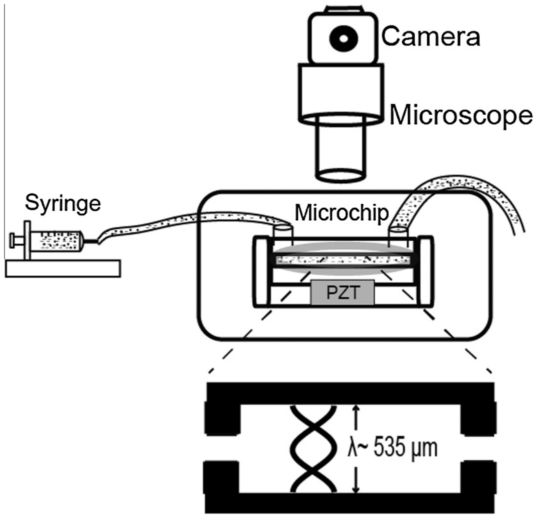

Fig. 2. Schematic representation of the experimental setup consisting of the silicon/glass microchip connected to the PZT transducer mounted below the microscope and the CCD camera. The detail (top-view) depicts the rectangular chamber and the acoustic standing-wave profile in the region of interest.

3.3. Accumulation time

The excitation voltage at the PZT (which is indirectly proportional to the applied pressure on the particle) was incrementally increased from 1 to 10 V. The motion of the particles was recorded for about two minutes at each voltage level and stored in a PC. The recorded videos were post-processed, and the motion of the particles was tracked in Matlab®. The image size is about 1080 × 1920, and particles in the image are visualized as black dots against a lighter background. A thresholding method was implemented to trace particles. The particle intensity profile was constructed by summation of all black dots along the channel width (the rows of image). The particle intensity profile demonstrates the number of particles in specific location along the width of the channel. With an activation of the PZT, the particles moved toward and accumulated at either the node or the antinode, where the corresponding region of interest (RoI) were selected. The particle intensity increased with time and saturated once the particles were trapped at either node or antinode. The time from PZT activation to maximum in particle intensity defined the particles' accumulation time.

4. Results

4.1. Microbeads

As shown in Fig. 3a, the solid polymer microbeads were randomly distributed across the chip and settled on the bottom plane of the channel when they were not subjected to acoustic standing-wave fields. With an activation of voltage (about 9 V_{pp}) across the PZT, the primary acoustic radiation forces dragged the polymer microbeads to the pressure node planes. As shown in Fig. 3b–f, the polymer microbeads aligned with the pressure node planes and formed two streamlines at $\lambda/4$ and $3\lambda/4$ as time progressed. The distribution of microbeads across the rectangular chamber was traced with respect to time. Fig. 4 presents the intensity profiles of the polymer microbeads that correspond to the images in Fig. 3. The intensity profiles clearly indicate that there are two pressure node planes, at about 130 μm (=$\lambda/4$) and at 400 μm (=$3\lambda/4$).

To calculate the accumulation time of microbeads, the region at the pressure node (at about 130 ± 40 μm) is considered a region of interest (RoI) for tracking particles accumulation over time, as illustrated in Fig. 4. The maximum intensity value in the RoI with respect to different time intervals is illustrated in Fig. 5. After activation of the PZT, the concentration of microbeads gradually increased to the maximum. The particle intensity reached a maximum, and the curve became saturated after the maximum. Thus, most of the polymer microbead population relocated at the pressure node plane at the point when the particle intensity reached its maximum. The time from PZT activation to the maximum particle intensity is the accumulation time, which is about 30 s for an electrical potential of about 9 V across the PZT.

The knowledge of accumulation time at varied electrical potential across the PZT is further employed for estimation of acoustic standing-wave field following Eq. (6) and microbeads characteristics reported in [40]. Both acoustic energy density, E_{ac}, and local

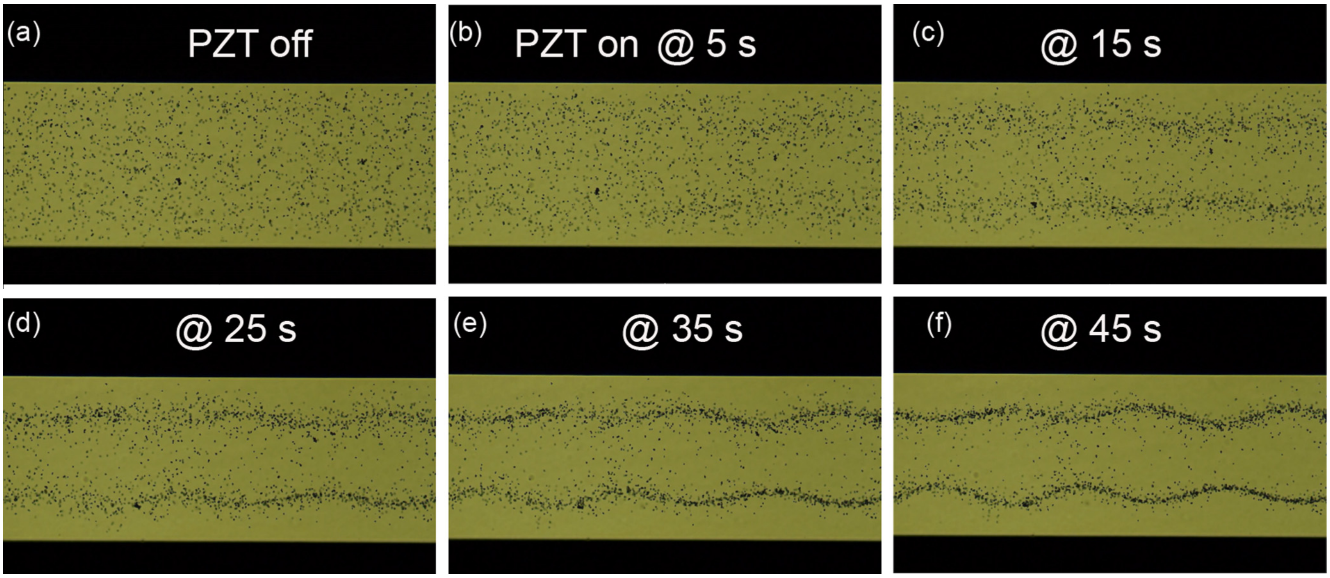

Fig. 3. The microscopic images focused along the rectangular chamber at different time intervals when the polymer microbeads were (a) not subjected to an acoustic standing-wave field and (b–f) subjected to an acoustic standing-wave field. As time progressed, the particles shifted toward the pressure node planes. The particles appear as black dots against a lighter background.

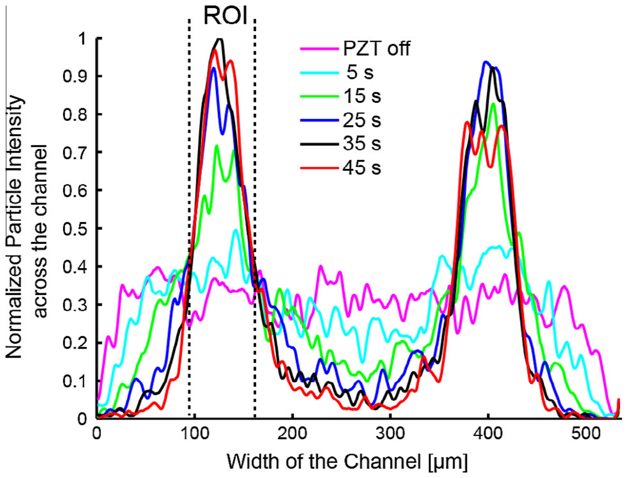

Fig. 4. Normalized intensity profiles of the polymer microbeads across the rectangle chamber at different time intervals, corresponding to images in Fig. 3.

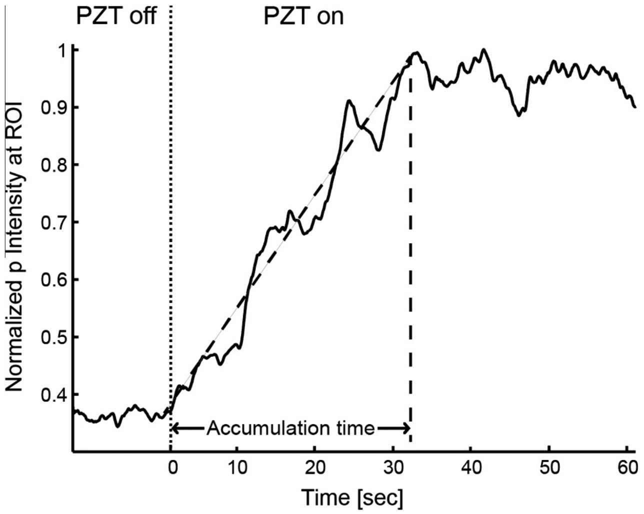

Fig. 5. Tracking the maximum intensity values around the ROI, as shown in (a)—that is, at one the pressure node plane at 133 ± 40 μm.

pressure amplitude, P_a, are estimated at electrical potential, U, between 3 and 10 V and reported in Fig. 6. The acoustic pressure amplitude, P_a, as expected depends linearly on the driving voltage, U. The value R^2 of the linear fit $P_a(U) = 14.86U + 21.67$ is equal to 0.98. At the maximum voltage considered in this study the acoustic energy density is 3 J/m^3 which correspond to the pressure amplitude of 165 kPa. These results are consistent with the previously reported values estimated using either individual particle tracking by Barnkob et al. [42], or light-intensity method by Barnkob et al. [40]. Worth mentioning is that at a pressure below 100 kPa microbubbles behave as a linear scatterers whereas in a range between approximately 100 kPa and 1 MPa polymer bubbles oscillation is nonlinear with second and higher order harmonics present in a spectra [46]. The fracturing of polymer microbubbles were extensively characterized in [47] and occurs at a peak negative pressure above 1 MPa at a frequency 2.2 MHz. As a result no fracturing, fragmentation or destruction of the microbubbles is expected at a pressure values considered in this study.

4.2. Polymer-shelled microbubbles

Fig. 7 illustrates the polymer-shelled microbubbles positions before and after they were subjected to a standing-wave acoustic field. Here the driving voltage across the PZT equaled 9 V. After the PZT activation, the polymer-shelled microbubbles were translated to antinode planes at the center ($w/2$) and near the walls (0 and w) along the channel. Once the polymer-shelled microbubbles were driven to the pressure antinode planes, they aggregated at different locations transverse to the initial direction of the radiation force. The reason for this aggregation is because of the weaker axial component of the 2D acoustic radiation force [42,48], but we also believe that the secondary acoustic force accelerates the accumulation. The intensity profiles of the polymer-shelled microbubbles' distribution in the chamber at time intervals corresponding to the images in Fig. 6 are given in Fig. 8. At the edges, the polymer-shelled microbubbles appear blurred and are not clearly

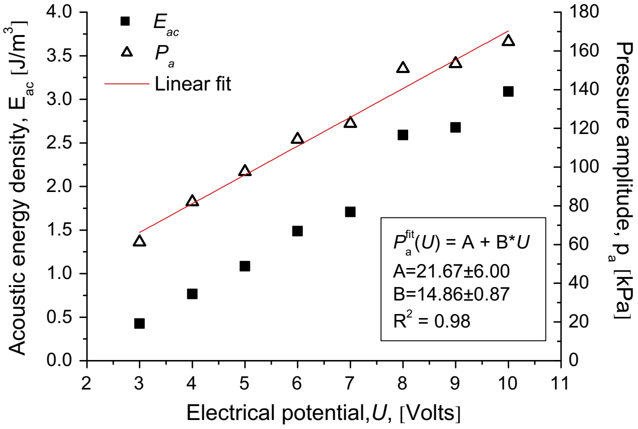

Fig. 6. Calibration of the acoustic standing-wave field inside the chamber. Acoustic energy density (squares) and corresponding pressure amplitude (triangles) are plotted with respect to the electrical potential applied to the PZT crystal. Solid line represents the linear fit of the pressure amplitude as a function of the driving voltage.

distinguishable from the wall background; for this reason, the polymer-shelled microbubbles at the edges were not tracked. As shown in Fig. 9, the RoI selected was 265 ± 40 μm (at $\lambda/2$) in order to measure the accumulation time of the polymer-shelled microbubbles.

The accumulation time of polymer microbeads and microbubbles at the node and antinode planes, respectively, versus the pressure amplitude is shown in Fig. 10a and b. It is evident that the accumulation time for both polymer-shelled microbubbles and polymer microbeads decreases as the pressure increases. The primary radiation forces generated by the PZT were too weak to drive the microbeads to the pressure node planes at a pressure below 60 kPa, which corresponds to the driving voltage less than 3 V. At pressure 165 kPa (10 V), the polymer-shelled microbubbles were driven to the antinode planes in less than half a second, while microbeads took approximately 26 s.

4.3. Mixed solution

The mixed solution (composed of both polymer-shelled microbubbles and polymer microbeads) was introduced into the microfluidic chip to attest the acoustophoresis separation between particles with a positive acoustic contrast factor (polymer microbeads) and others with a negative acoustic contrast factor (polymer-shelled microbubbles). As shown in Fig. 11, the polymer-shelled microbubbles were collected and focused in the antinode plane (located in the lower plane), while microbeads were situated in the pressure node plane (located in the upper plane) in the presence of an ultrasound standing wave. The density of the polymer-shelled microbubbles was half the density of water, the weight of the displaced water was greater than the weight of the particle, and the buoyancy forces moved the polymer-shelled microbubbles to the upper surface of the chip. On the other hand, the density of microbeads was slightly greater than the density of water, and the weight of the displaced water was greater than the weight of the microbeads; thus, microbeads were deposited in the bottom plane of the chip. This is visualized clearly in Fig. 11b and c, where polymer microbeads and polymer-shelled microbubbles can be seen concentrated in different planes along the z-axis.

5. Discussion

In this study, we examined the movements (directions and velocities) of polymer-shelled microsize gas-core bubbles with respect to radiation force in acoustic standing-wave fields. Polymer microbeads (solid microparticles) were employed to mimic the acoustic behavior of red blood cells and also allow us to estimate the acoustic energy density and peak pressure inside the standing wave resonator.

In contrast to solid microparticles, such as plain polymer microbeads [42], the polymer-shelled microbubbles have shown the tendency to be translated and trapped at the pressure antinode planes in ways similar to lipid (fat) particles [27], oil droplets [30], elastomeric particles [32], and hollow and glass-shelled core particles [33]. Although the glass-shelled core particles' movement can extend to the motion of UCAs, a scenario mentioned by Leibacher et al. [33], several other phenomena should be taken into account for UCAs, such as resonance frequency, damping, and compressibility. Indeed, the compressibility of glass-shelled core particles is far less than the compressibility of UCAs.

According to the theory, for highly compressible μm-size gas bubbles suspended in water media, the acoustic contrast factor, Φ, has a huge negative value, about −5640. Thus, gas bubbles are naturally negative acoustic contrast particles, and they certainly

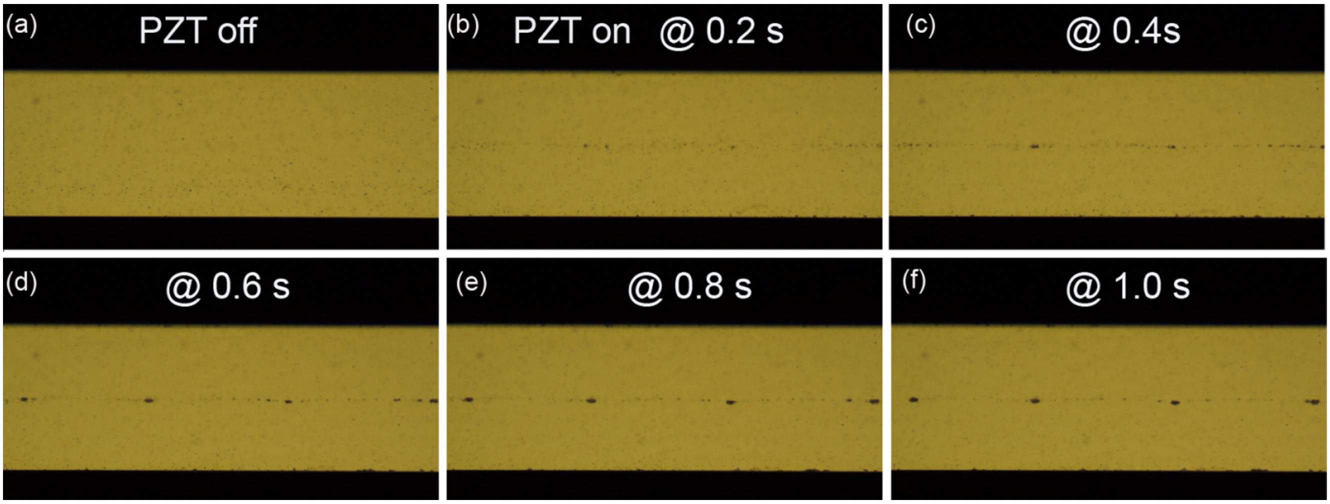

Fig. 7. The microscopic images of polymer-shelled microbubbles (represented by black dots) in a rectangular chamber at different time intervals. (a) When the polymer-shelled microbubbles are not subjected to an acoustic standing-wave field and (b–f) when they are subjected to an acoustic ultrasound standing-wave field at an intervals of 0.2, 0.4, 0.6, 0.8, and 1.0 s respectively.

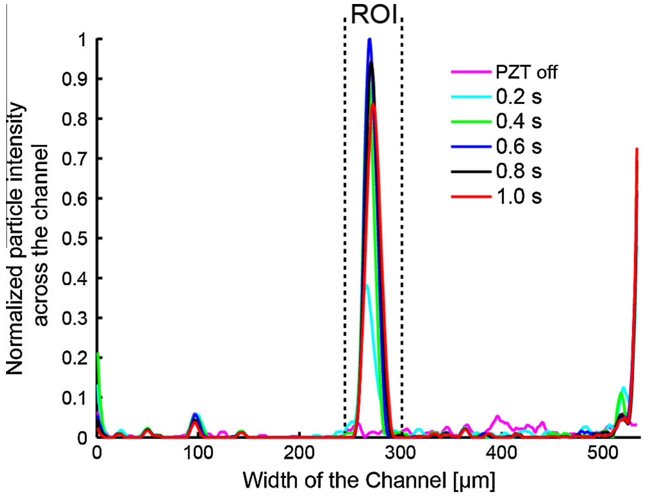

Fig. 8. Normalized intensity profiles of the polymer-shelled microbubbles across the rectangular chamber at different time intervals, corresponding to the images given in Fig. 6.

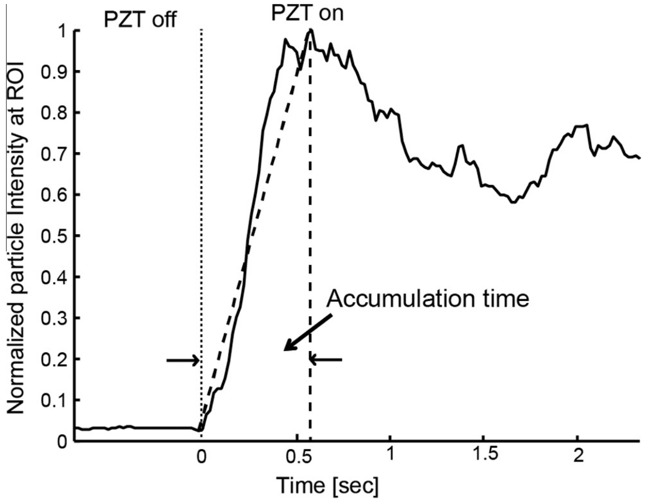

Fig. 9. Tracking the maximum intensity values around 265 ± 40 μm (i.e., around pressure antinode planes).

have a tendency to move toward the pressure antinode under the radiation force in an ultrasound standing wave [18]. However, rapid dissolution of gas in water makes it more difficult to document this phenomenon experimentally in unprotected microsize gas bubbles (e.g., a three-micron-size free gas bubble diffused in a liquid within 0.02 s [49]), and they are less useful for practical applications.

As mentioned in the introduction, thin-shelled microbubbles (Optison®) have also disappeared rapidly in high-intensity ultrasound standing-wave fields during cell viability studies [35]. In addition, the resonance frequencies of these UCAs varied within the 1–5 MHz range owing to differences in size distribution (poly-dispersion) [49]. Given excitation within this frequency range, the bigger bubbles (i.e. resonance frequency lower than excitation frequency) move to the pressure node, while the smaller bubbles (i.e. resonance frequency higher than excitation frequency) move to the pressure antinode [18]. It is therefore challenging to study the polydispersed thin-shelled microbubbles in acoustophoresis. On the other hand, the polymer-shelled microbubbles utilized in this study are relatively monodispersed in size and possess higher mechanical stability than thin-shelled microbubbles do. The resonance frequency of polymer-shelled microbubbles at about 12 MHz [36] is far from the excitation frequency (2.8 MHz) generated in this study by the PZT attached to the microchip, and the polymer-shelled microbubbles did not exhibit any resonance effect (chaotic motion) during the experiments. Moreover, these microbubbles remained intact for longer periods in the actuation filed. In other words, the polymer-shelled microbubbles were not destroyed at any pressure values considered in this study.

The acoustic contrast factor, Φ, for currently reported acoustic contrast particles (both negative and positive) such as blood cells, microbeads, lipid particles, oil droplets, and elastomer particles falls between −1 and 1. This is because the density difference and the compressibility difference from the surrounding fluid media are not significant. For example, the monopole scattering coefficient (i.e., compressibility factor), f_1, and the dipole scattering coefficient (i.e., density factor), f_2, of an oil droplet are −0.44 and −0.07, respectively, and the resulting Φ is −0.18 [30]. In the case of polymer-shelled microbubbles, the Φ is estimated to be −60.7, and it is several orders of magnitude greater than the Φ of currently reported negative contrast particles, even if the Φ, owing to a thick stabilizing shell, is appreciably decreased relative to that of free gas bubbles. The total density of a polymer-shelled microbubble, including its gas core, is about half the density of water. As a result, f_2 becomes positive, and its value is equal +0.4. The polymer shell is compressible, but the compressibility of the gas core is several magnitudes higher than that of the shell. This renders f_1 negative, making its value about −181.4. Compressibility therefore plays a major role in allowing polymer-shelled microbubbles to behave as negative acoustic contrast particles.

Moreover, the polymer-shelled microbubbles respond more quickly to the acoustic radiation force than the polymer microbeads do. They relocate at the pressure antinode much faster

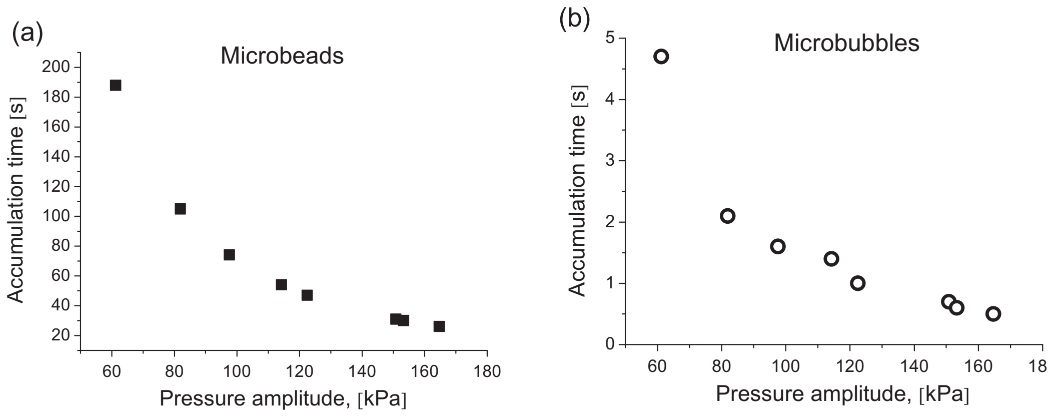

Fig. 10. The accumulation time of microbeads (a) at pressure node and microbubbles (b) at pressure antinode plane with respect to the pressure amplitude.

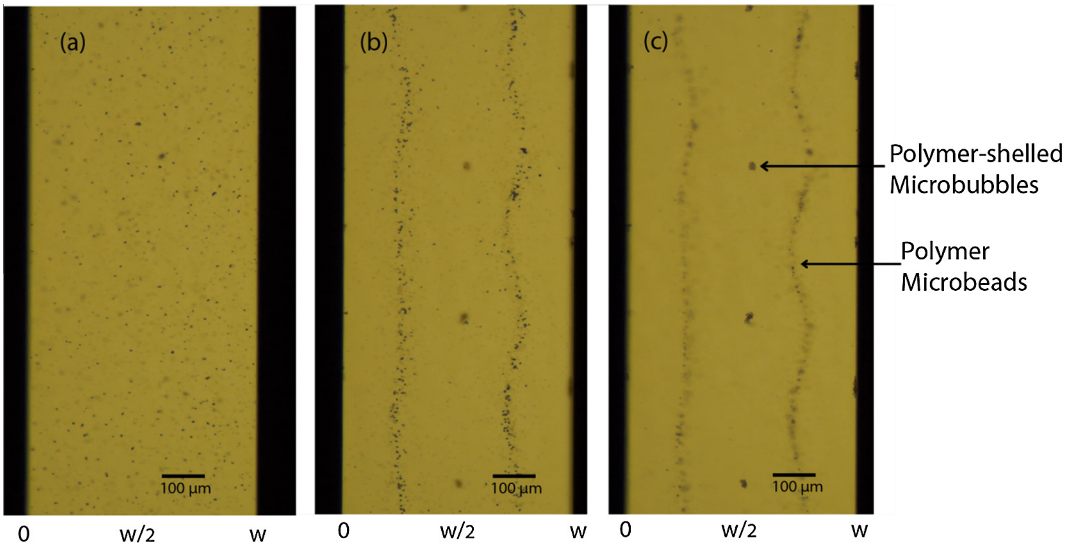

Fig. 11. Microscopic images of mixed polymer-shelled microbubbles' and solid polymer microbeads' suspension in the microchip (a) before and (b and c) after being subjected to acoustic standing-wave fields. Owing to the density differences between bubbles and solid particles, they aligned in different planes. In (b) the bubbles are out of focus at pressure antinode planes, and the beads at pressure node planes are in focus, whereas in (c) the beads are out of focus at nodes, and the bubbles are in focus.

(typically around 40 times faster) than microbeads do at the pressure node. Fig. 10a and b illustrates that the relocation time decreases as the pressure amplitude increases. Both microbubble and microbeads experience the same acoustic radiation pressure at the same driving voltage across the PZT; however, greater particle velocity is obtained for the polymer-shelled microbubbles. This can be explained by Eq. (1), which indicates that the radiation force, F^{y}_{rad}, acting on the particles is directly proportional to the volume of the particle, V, the square of the pressure amplitude, p^2, the frequency, f, and the acoustic contrast factor, Φ. The volume of the microbeads (5.23×10^{-16}) is 2.2 times higher than the volume of the polymer-shelled microbubbles (2.29×10^{-16}), while the Φ of the polymer-shelled microbubbles is approximately 120 times higher than that of the polymer microbeads. The corresponding radiation force acting on the polymer-shelled microbubbles is approximately 146 times higher than the radiation force acting on the plain polymer microbeads.

The forces acting on the polymer-shelled microbubbles in the transverse direction are much stronger than those evident for the plain polymer particles, as illustrated in Fig. 7. The transverse component is very prominent, while the axial motion is almost below the threshold for plain particles. The transverse component, because of the non-uniform standing-wave along the channel, produced a 2-D standing wave [48], although we intended to produce a 1-D standing wave across the channel. Moreover, both the interaction between particles and the particle–wall interaction are much more prominent for microbubbles, a phenomenon that is not accounted for in this study (the Gor'kov model assumes only single-particle motion in a 1-D standing wave and does not account for other effects, such as a 2-D wave or wall interactions).

The current study is limited to no-flow conditions that is, the particles are free from flow-related effects, such as microstreaming. As a result, the buoyancy forces exerted by the fluid on the polymer-shelled microbubbles bring them to the upper surface of the channel, while the same forces exerted on the microbeads moved them to the chip's bottom plane (Fig. 11).

5.1. Possible clinical applications

Recent advances in surface chemistry make it possible to modify the encapsulated shell in order to anchor ligands and selectively target the diseased tissue or organ. The bubbles are today pure blood-pool contrast media and the possible targeting cells are blood-, endothelial-, and macrophage-like cells hiding in the liver and the spleen [7,50]. Reported in this article polymer-shelled microbubbles can easily be decorated with dyes [37], ligands (such as RGD peptides [51]), and antibodies [52] in order to target the endothelial cells and liver inflammation where the affinity between functionalized microbubbles and targeted cells is crucial. These polymer-shelled microbubbles can be potentially utilized in bioanalytical applications. For example, the functionalized microbubbles bounded to the cells can be potentially trapped at the pressure antinode at a pressure level as low as 60 kPa, leaving free cells unaffected.

The polymer-shelled microbubbles exhibited stable both linear and nonlinear oscillations below 1 MPa. Moreover, microbubbles can be disrupted without forming secondary free gas bubbles at high acoustic pressure of about 1 MPa [47], in contrast to thin-shelled and even other types of polymer-shelled microbubbles [53]. This disruption process is attractive for reversible sonoporation applications [54]. In molecular and genetic disease, an acoustophoretic single-cell lysis characterization has been suggested [55]. The acoustic lysis procedure requires long (approximately 50 s) high-pressure ultrasound exposures, resulting in significant heating and denaturation of intracellular components [55]. In the presence of microbubbles, the acoustic cavitation pressure threshold is reduced, as is the exposure time needed.

6. Conclusion

The key knowledge this paper presents is insight into the physical properties and behavior of stable polymer-shelled microsize gas bubbles in acoustic standing-wave fields of low megahertz frequency of 2.8 MHz and pressure below 165 kPa. Theoretical considerations and the calculated acoustic contrast factor ($\Phi = -60.7$) hinted that the primary radiation force drags the polymer-shelled microbubbles to the pressure antinode planes; this was experimentally confirmed. The polymer-shelled microbubbles translated to the pressure antinode planes within half a second, corresponding to an acoustic radiation force 146 times higher than that for plain polymer beads, Moreover, these microbubbles could be separated from solid particles. The high negative Φ of polymer-shelled microbubbles can be beneficial in performing bioanalytical applications *in vitro* with the help of acoustophoresis methods. This experimental evidence of stabilized gas bubbles' behavior in an acoustic standing-wave resonator can be further extended to cell sorting, cell lysis, or bioaffinity studies.

Acknowledgements

Authors would like to appreciate Muhammed Asim Faridhhi, Mathias Ohlin and Ida Sadat Iranmanesh for their thorough support and enthusiastic discussions. The study was partly covered by EU-grants (3MiCRON) and strategic money from Karolinska Institute.

References

[1] J. Ophir, K.J. Parker, Contrast agents in diagnostic ultrasound, Ultrasound Med. Biol. 15 (1989) 319–333.
[2] R. Gramiak, P.M. Shah, Echocardiography of the aortic root, Invest. Radiol. 3 (1968) 356–366.
[3] S.B. Feinstein, P.M. Shah, R.J. Bing, S. Meerbaum, E. Corday, B.-L. Chang, G. Santillan, Y. Fujibayashi, Microbubble dynamics visualized in the intact capillary circulation, J. Am. Coll. Cardiol. 4 (1984) 595–600.
[4] M. Schneider, SonoVue, a new ultrasound contrast agent, Eur. Radiol. 9 (1999) S347.
[5] M.A. Wheatley, B. Schrope, P. Shen, Contrast agents for diagnostic ultrasound: development and evaluation of polymer-coated microbubbles, Biomaterials 11 (1990) 713–717.
[6] A.L. Klibanov, Microbubble contrast agents: targeted ultrasound imaging and ultrasound-assisted drug-delivery applications, Invest. Radiol. 41 (2006) 354–362.
[7] K. Ferrara, R. Pollard, M. Borden, Ultrasound microbubble contrast agents: fundamentals and application to gene and drug delivery, Biomed. Eng. 9 (2007).
[8] J.R. Lindner, J. Song, J. Christiansen, A.L. Klibanov, F. Xu, K. Ley, Ultrasound assessment of inflammation and renal tissue injury with microbubbles targeted to P-selectin, Circulation 104 (2001) 2107–2112.
[9] J.J. Rychak, A.L. Klibanov, K.F. Ley, J.A. Hossack, Enhanced targeting of ultrasound contrast agents using acoustic radiation force, Ultrasound Med. Biol. 33 (2007) 1132–1139.
[10] P.A. Dayton, J.S. Allen, K.W. Ferrara, The magnitude of radiation force on ultrasound contrast agents, J. Acoust. Soc. Am. 112 (2002) 2183–2192.
[11] L. Rayleigh, XXXIV. On the pressure of vibrations, Lond., Edinburgh, Dublin Philos. Mag. J. Sci. 3 (1902) 338–346.
[12] M. Fatemi, J.F. Greenleaf, Vibro-acoustography: an imaging modality based on ultrasound-stimulated acoustic emission, Proc. Natl. Acad. Sci. USA 96 (1999) 6603–6608.
[13] F. Sebag, J. Vaillant-Lombard, J. Berbis, V. Griset, J. Henry, P. Petit, C. Oliver, Shear wave elastography: a new ultrasound imaging mode for the differential diagnosis of benign and malignant thyroid nodules, J. Clin. Endocrinol. Metab. 95 (2010) 5281–5288.
[14] K. Nightingale, M.S. Soo, R. Nightingale, G. Trahey, Acoustic radiation force impulse imaging: in vivo demonstration of clinical feasibility, Ultrasound Med. Biol. 28 (2002) 227–235.
[15] R. Muthupillai, D. Lomas, P. Rossman, J. Greenleaf, A. Manduca, R. Ehman, Magnetic resonance elastography by direct visualization of propagating acoustic strain waves, Science 269 (1995) 1854–1857.
[16] W.F. Walker, F.J. Fernandez, L.A. Negron, A method of imaging viscoelastic parameters with acoustic radiation force, Phys. Med. Biol. 45 (2000) 1437.
[17] W. Coakley, G. Whitworth, M. Grundy, R. Gould, R. Allman, Ultrasonic manipulation of particles and cells. Ultrasonic separation of cells, Bioseparation 4 (1994) 73–83.
[18] F. Blake Jr., Bjerknes forces in stationary sound fields, J. Acoust. Soc. Am. 21 (1949) 551.
[19] L.A. Crum, Bjerknes forces on bubbles in a stationary sound field, J. Acoust. Soc. Am. 57 (1975) 1363–1370.
[20] A.A. Doinikov, Translational motion of a spherical bubble in an acoustic standing wave of high intensity, Phys. Fluids 14 (1994–present) 1420–1425.
[21] A. Kundt, O. Lehmann, Über longitudinale Schwingungen and Klangfiguren in zylindrischen Flüssigkeitssäulen, Ann. Phys. 135 (1874) 1–12.
[22] L. Gor'Kov, On the forces acting on a small particle in an acoustical field in an ideal fluid, in: Soviet Physics Doklady, 1962, p. 773.
[23] K. Yosioka, Y. Kawasima, Acoustic radiation pressure on a compressible sphere, Acta Acust. United Acust. 5 (1955) 167–173.
[24] A. Lenshof, T. Laurell, Emerging clinical applications of microchip-based acoustophoresis, J. Assoc. Lab. Autom. 16 (2011) 443–449.
[25] A. Lenshof, C. Magnusson, T. Laurell, Acoustofluidics 8: applications of acoustophoresis in continuous flow microsystems, Lab Chip 12 (2012) 1210–1223.
[26] M. Grösch, W. Burger, B. Handl, O. Doblhoff-Dier, T. Gaida, C. Schmatz, Ultrasonic separation of suspended particles – Part III: Application in biotechnology, Acta Acust. United Acust. 84 (1998) 815–822.
[27] F. Petersson, A. Nilsson, C. Holm, H. Jönsson, T. Laurell, Separation of lipids from blood utilizing ultrasonic standing waves in microfluidic channels, Analyst 129 (2004) 938–943.
[28] F. Petersson, L. Åberg, A.-M. Swärd-Nilsson, T. Laurell, Free flow acoustophoresis: microfluidic-based mode of particle and cell separation, Anal. Chem. 79 (2007) 5117–5123.
[29] C. Grenvall, P. Augustsson, J.R. Folkenberg, T. Laurell, Harmonic microchip acoustophoresis: a route to online raw milk sample precondition in protein and lipid content quality control, Anal. Chem. 81 (2009) 6195–6200.
[30] H. Wang, Z. Liu, S. Kim, C. Koo, Y. Cho, D.-Y. Jang, Y.-J. Kim, A. Han, Microfluidic acustophoretic force based low-concentration oil separation and detection from the environment, Lab Chip 14 (2014) 947–956.
[31] K.W. Cushing, M.E. Piyasena, N.J. Carroll, G.C. Maestas, B.A. López, B.S. Edwards, S.W. Graves, G.P. López, Elastomeric negative acoustic contrast particles for affinity capture assays, Anal. Chem. 85 (2013) 2208–2215.
[32] C.W. Shields IV, L.M. Johnson, L. Gao, G.P. López, Elastomeric negative acoustic contrast particles for capture, acoustophoretic transport, and confinement of cells in microfluidic systems, Langmuir 30 (2014) 3923–3927.
[33] I. Leibacher, W. Dietze, P. Hahn, J. Wang, S. Schmitt, J. Dual, Acoustophoresis of hollow and core-shell particles in two-dimensional resonance modes, Microfluid. Nanofluid. 16 (2014) 513–524.
[34] L. Hoff, Acoustic Characterization of Contrast Agents for Medical Ultrasound Imaging, Springer, 2001.
[35] S. Khanna, N.N. Amso, S.J. Paynter, W.T. Coakley, Contrast agent bubble and erythrocyte behavior in a 1.5-MHz standing ultrasound wave, Ultrasound Med. Biol. 29 (2003) 1463–1470.
[36] D. Grishenkov, C. Pecorari, T.B. Brismar, G. Paradossi, Characterization of acoustic properties of PVA-shelled ultrasound contrast agents: linear properties (part I), Ultrasound Med. Biol. 35 (2009) 1127–1138.
[37] F. Cavalieri, A. El Hamassi, E. Chiessi, G. Paradossi, Stable polymeric microballoons as multifunctional device for biomedical uses: synthesis and characterization, Langmuir 21 (2005) 8758–8764.
[38] S. Sirsi, M. Borden, Microbubble compositions, properties and biomedical applications, Bubble Sci., Eng. Technol. 1 (2009) 3–17.
[39] D. Grishenkov, A. Gonon, E. Weitzberg, J. Lundberg, J. Harmark, B. Cerroni, G. Paradossi, B. Janerot-Sjoberg, Ultrasound contrast agent loaded with nitric oxide as a theranostic microdevice for myocardial ischemia, J. Drug Des., Dev. Ther. 2015 (9) (2015) 2409–2419.
[40] R. Barnkob, I. Iranmanesh, M. Wiklund, H. Bruus, Measuring acoustic energy density in microchannel acoustophoresis using a simple and rapid light-intensity method, Lab Chip 12 (2012) 2337–2344.
[41] M. Wiklund, H.M. Hertz, Ultrasonic enhancement of bead-based bioaffinity assays, Lab Chip 6 (2006) 1279–1292.
[42] R. Barnkob, P. Augustsson, T. Laurell, H. Bruus, Measuring the local pressure amplitude in microchannel acoustophoresis, Lab Chip 10 (2010) 563–570.
[43] P.A. Fernandes, G. Tzvetkov, R.H. Fink, G. Paradossi, A. Fery, Quantitative analysis of scanning transmission X-ray microscopy images of gas-filled PVA-based microballoons, Langmuir 24 (2008) 13677–13682.
[44] M. Poehlmann, D. Grishenkov, S.V. Kothapalli, J. Härmark, H. Hebert, A. Philipp, R. Hoeller, M. Seuss, C. Kuttner, S. Margheritelli, On the interplay of shell structure with low-and high-frequency mechanics of multifunctional magnetic microbubbles, Soft Matter 10 (2014) 214–226.
[45] M. Wiklund, J. Toivonen, M. Tirri, P. Hänninen, H.M. Hertz, Ultrasonic enrichment of microspheres for ultrasensitive biomedical analysis in confocal laser-scanning fluorescence detection, J. Appl. Phys. 96 (2004) 1242–1248.
[46] C. Sciallero, D. Grishenkov, S. Kothapalli, L. Oddo, A. Trucco, Acoustic characterization and contrast imaging of microbubbles encapsulated by polymeric shells coated or filled with magnetic nanoparticles, J. Acoust. Soc. Am. 134 (2013) 3918–3930.
[47] D. Grishenkov, C. Pecorari, T.B. Brismar, G. Paradossi, Characterization of acoustic properties of PVA-shelled ultrasound contrast agents: linear properties (part II), Ultrasound Med. Biol. 35 (2009) 1139–1147.
[48] S. Hagsäter, A. Lenshof, P. Skafte-Pedersen, J.P. Kutter, T. Laurell, H. Bruus, Acoustic resonances in straight micro channels: beyond the 1D-approximation, Lab Chip 8 (2008) 1178–1184.
[49] N. De Jong, M. Emmer, A. Van Wamel, M. Versluis, Ultrasonic characterization of ultrasound contrast agents, Med. Biol. Eng. Comput. 47 (2009) 861–873.
[50] A.L. Klibanov, Targeted delivery of gas-filled microspheres, contrast agents for ultrasound imaging, Adv. Drug Deliv. Rev. 37 (1999) 139–157.
[51] M. Tortora, L. Oddo, S. Margheritelli, G. Paradossi, Design of novel polymer shelled ultrasound contrast agents: towards an ultrasound triggered drug delivery, in: Ultrasound Contrast Agents, Springer, 2010, pp. 25–39.
[52] R. Villa, B. Cerroni, L. Viganò, S. Margheritelli, G. Abolafio, L. Oddo, G. Paradossi, N. Zaffaroni, Targeted doxorubicin delivery by chitosan-galactosylated modified polymer microbubbles to hepatocarcinoma cells, Colloids Surf., B: Biointerfaces 110 (2013) 434–442.
[53] S.H. Bloch, M. Wan, P.A. Dayton, K.W. Ferrara, Optical observation of lipid-and polymer-shelled ultrasound microbubble contrast agents, Appl. Phys. Lett. 84 (2004) 631–633.
[54] K. Kooiman, M. Foppen-Harteveld, A.F. van der Steen, N. de Jong, Sonoporation of endothelial cells by vibrating targeted microbubbles, J. Control. Release 154 (2011) 35–41.
[55] R.B. Brown, J. Audet, Current techniques for single-cell lysis, J. R. Soc. Interface 5 (2008) S131–S138.